



島根大学学術情報リポジトリ
S W A N
Shimane University Web Archives of kNnowledge

Title

Digital materials design by thermal-fluid science for multi-metal additive manufacturing

Author(s)

Junji Shinjo, Chinnapat Panwisawas

Journal

Acta Materialia Volume 210, 116825

Published

15 May 2021

URL

<https://doi.org/10.1016/j.actamat.2021.116825>

この論文は出版社版ではありません。
引用の際には出版社版をご確認のうえご利用ください。

Digital Materials Design by Thermal-Fluid Science for Multi-Metal Additive Manufacturing

Junji Shinjo^a and Chinnapat Panwisawas^{a,b,c,*}

^aNext Generation Tatara Co-Creation Centre (NEXTA), Shimane University, 1060, Nishikawatsu, Matsue 690-8504, Japan

^bNISCO UK Research Centre, School of Leicester, University of Leicester, Leicester LE1 7RH, United Kingdom

^cDepartment of Materials, University of Oxford, Oxford OX1 3PH, United Kingdom

*Corresponding author. chinnapat.panwisawas@leicester.ac.uk

Abstract

Metal additive manufacturing is promising for designing advanced metallic parts of complex geometries. The challenge lies in process control on melt flow dynamics, alloy mixing and vapour mass loss, which is significantly vital for the final quality. A high-fidelity thermal-solutal-fluid modelling approach including accurate tracking of surface shape, thermo-capillary dynamics and vaporisation has been developed. Multi-species formulations are also included for multi-metal simulation. Using this method, the physical link between metal vapour mass loss and melt flow process for 21 transition metals and 3 binary alloys is investigated. The mass loss rate is governed by a fluid dynamic parameter of Reynolds number with a simple proportional correlation linked with thermal-fluid behavior of the melt pool, and convective mixing further complicates the behaviour in *in-situ* binary alloying. The digital materials approach is effective in understanding complex interdependent thermal-fluid flow dynamics and can advance process-based materials design.

Keywords: Thermal-solutal-fluid modeling, Vapor mass loss, Multi-metal additive manufacturing, Melt flow process

1. Introduction

Metal additive manufacturing (AM) is an emerging digital technology which possesses a large degree of design freedom to fabricate intricate three-dimensional structures with minimum waste/scrappage and aimed at minimum subsequent post-treatment [1]. The AM application in metallurgy perceives a great attention from various industries, such as aerospace, automotive, nuclear and biomedical sectors, which indicates a large potential of this technology [1-4]. For these applications, various transition metals are used as base metals for electrical, functional or structural materials.

During the metal AM process, a number of complicated thermal-fluid behaviours at liquid-vapour interface occur which include laser heating, melting, re-melting, vaporisation (metal vapour dynamics), melt fluid flow, keyholing, spatter or entrainment of melt jet, denudation, and particle ejection due to vapour plume [1,5-7]. Resultant microstructures will be strongly affected by these inter-related multi-physics phenomena. Experiments have revealed complicated interactions of the above dynamics and especially recent real-time visualisation methods such as X-ray imaging have contributed much to enable time-resolved observation [8-15]. Accurate 3D observation is, however, still difficult since the scales are small and the relevant phenomena are highly unsteady. For example, the *in-situ* chemical changes and metal vapour dynamics due to the volatile elements induced by AM, which is one of the over-arching goals in this study, has not yet been available.

Given the improved computational power, numerical simulation based on thermal-solutal-fluid flow formulation has been becoming a powerful tool to elucidate detailed multi-scale physics of metal AM [7,16-28]. For example, melt pool/keyhole formation [16-24,28] and spattering and denudation [19,20,26] were reproduced in simulation. Material removal due to laser ablation has been investigated from a fundamental viewpoint for a better modeling [29,30]. Mukherjee *et al.* [21] discussed the process parameters using a simple computational approach. Recently, Khairallah *et al.* [7] used a high-fidelity approach to see the interdependency of relevant interfacial phenomena. Improvement of the computational methods relevant to AM is intensively continuing to include complicated interactions of relevant phenomena in a more realistic and rigorous way such as

capturing powder motion with heating and melting [31-33], indicating the active research interests in this field.

These experimental and computational studies have set important milestones. However, there are still some remaining unsolved problems that have not been well understood yet. One issue is the metal vapour dynamics and mass loss characteristics in metal AM, which is significant in determining the local alloy structures and its thermal, mechanical and chemical properties [1]. For example, Ti-6Al-4V, widely used for biomedical and aerospace applications, loses elements preferentially during high-power laser melting and vaporisation, which alters the local composition and may lead to unfavourable mechanical properties [34]. Elahinia *et al.* [35] suggested that NiTi, a shape-memory and super-elastic alloy, generally tends to lose more Ni due to preferential vaporisation under high-energy AM conditions, which leads to different transformation temperatures and different mechanical behaviour. High-entropy alloys [36], which are unlike conventional alloys and have multiple principle elements, are recently of great interest and may be more directly prone to the uneven mass loss when AM is applied. These examples highlight the significance and impact of the investigation on the mass loss in AM. At the current stage, the difference of mass loss among elements is still unknown, which therefore has an impact in designing alloys.

Another unresolved issue is the relevance of mass loss to the process parameters such as Reynolds and Péclet numbers, by which the melt flow dynamics is characterised as a function of materials. AM involves small-scale as well as rapid and repeated melting/solidification phenomena, and in order to address the above-mentioned issue of mass loss in alloys under different heating conditions, considerations for highly transient and unsteady processes are definitely needed. Mukherjee *et al.* [21] investigated the effect of process parameters, but the simulation method was simplified and vaporisation was not comprehensively considered. In contrast to the traditional materials design to solve the interaction of atomic bonds and energy, there is a pressing need to have chemistry-process materials design tool for multi-metal AM. These points have motivated the present study.

In this paper, by newly using a high-fidelity simulation method with multiple chemical species, the aims are to investigate the mass loss characteristics of different elemental powders and also binary *in-situ* alloys under AM conditions, and to identify the effect of thermal-fluid parameters in the melt

flow and metal vapour dynamics. Computational methodology for AM so far has still lacked formulations for the key features that must be precisely captured in multi-metal AM. They include melted surface shape tracking with volume/mass conservation, thermo-capillary dynamics, surface vaporisation and multi-species tracking with convection and diffusion. In order to understand the AM physics, these numerical formulations are considered in this study as described in Section 2. Only very recently such a modelling effort has begun to be pursued in AM simulation [7,32,33,37]. The present method is therefore a state of the art approach to tackle AM issues including vapour dynamics and multi-metal effects. By this study, it is expected that relevant processes will be understood toward designing alloy systems using metal AM in various technological applications.

2. Numerical Methods

2.1. Thermal-Solutal-Fluid Flow

The key features that must be precisely captured in multi-metal AM are melted surface shape-tracking with volume/mass conservation, thermo-capillary dynamics, surface vaporisation and multi-species tracking with convection and diffusion. For each issue, respectively, the CLSVOF (coupled level-set and volume-of-fluid) method, the continuum surface force method, vaporisation jump conditions and species mass fraction equations are considered in this study, as described below. In most metallurgical simulations of so far, these effects have not been considered rigorously, and only very recently such an effort has begun to be pursued [7,32,33,37]. The present method enables solving AM simulation issues including vapour dynamics and multi-metal effects.

Our in-house code TATM-MEX [38-42] is applied to AM to investigate the compositional dependence and multi-species (multi-metal) thermal-fluid flow calculation. The governing equations to be solved are the Navier-Stokes equations coupled with phase change, which are for continuity, momentum conservation, energy conservation and chemical concentration conservation, given as [38-42]

$$\begin{aligned}
\frac{\partial \rho}{\partial t} + (\mathbf{u} \cdot \nabla) \rho &= -\rho \nabla \cdot \mathbf{u} \\
\frac{\partial \mathbf{u}}{\partial t} + (\mathbf{u} \cdot \nabla) \mathbf{u} &= -\frac{\nabla p}{\rho} + \mathbf{Q}_u + \mathbf{F}_{u,surf} \\
\frac{\partial T}{\partial t} + (\mathbf{u} \cdot \nabla) T &= -\frac{p \nabla \cdot \mathbf{u}}{\rho c_p} + Q_T + \frac{1}{\rho c_p} q_L \\
\frac{\partial Y_i}{\partial t} + (\mathbf{u} \cdot \nabla) Y_i &= \frac{1}{\rho} \nabla \cdot (\rho D \nabla Y_i)
\end{aligned} \tag{1}$$

where ρ is the density, \mathbf{u} is the velocity, T is the temperature, p is the pressure and Y_i is the mass fraction of species i . The inclusion of species mass fraction equations enables to track mixing of species in the vapour and the liquid. The ambient gas is air and the species i include N_2 , O_2 and the metal element. \mathbf{Q}_u represents the Newtonian viscous force, given by

$$Q_{u,i} = \frac{1}{\rho} \frac{\partial \tau_{ij}}{\partial x_j}, \quad \tau_{ij} = \mu \left(\frac{\partial u_i}{\partial x_j} + \frac{\partial u_j}{\partial x_i} \right) - \frac{2}{3} \mu \nabla \cdot \mathbf{u} \delta_{ij}. \tag{2}$$

$\mathbf{F}_{u,surf}$ represents the interfacial surface tension force including the Marangoni effect, formulated by the continuum surface force method [38-42]. Q_T represents the heat transport, including heat conduction by Fourier's law, enthalpy transport by mass diffusion, viscous work, latent heat for phase-change and radiation,

$$Q_T = \frac{1}{\rho c_p} \left[\nabla \cdot (\lambda \nabla T) - \nabla \cdot (\rho \sum h_i Y_i V_i) + \frac{\partial \tau_{ij} u_i}{\partial x_j} - \frac{D \sum \rho Y_i \Delta h_i}{Dt} \right] + \varepsilon \sigma_{SB} (T^4 - T_0^4) |\nabla \phi| \tag{3}$$

where V_i is the diffusion velocity formulated by Fick's law. Δh_i is the latent heat of species i .

Radiation is included on the heated metal surface identified by the gradient of the colour function $|\nabla \phi|$, with σ_{SB} the Stefan-Boltzmann constant and ε the emissivity. q_L is the volumetric laser heat input given by Xu *et al.*'s model [43], which mimics ray tracing and keyhole profile. The volumetric heat source is modelled as

$$q_L = \frac{3\eta_L Q_L}{\pi(1-e^{-3})(E+F)} \left(\frac{1-\chi}{z_e - z_i} z + \frac{\chi z_e - z_i}{z_e - z_i} \right) \exp\left(-\frac{3r^2}{r_0^2(z)}\right), \tag{4}$$

where Q_L is the laser power in W, η_L is the absorption coefficient, z is the coordinate along the laser beam, z_e is the laser inlet position, z_i is the laser bottom position, r_0 is the radius distribution between

the inlet and bottom, χ is the proportion factor, and E and F are geometrical factors determined by z_e and z_i .

In typical AM simulations, the vapour mass has not been accurately incorporated. Here, in order to accurately estimate the mass loss due to vaporisation, a volume/mass conserving interface capturing method is needed. The level-set (LS) method [44] is often used for accurate shape tracking for surface tension estimation, but it is known that the liquid volume/mass is erroneously lost. To assure the volume/mass conservation, a volume-of-fluid method must be combined (CLSVOF) [38,45]. Here, the MARS (Multi-interface Advection and Reconstruction Solver) method [38,40], a variant of volume of fluid (VOF) method, is combined to assure that the interface shape between the liquid/gas phase can be accurately captured by the LS method while assuring the volume/mass conservation by the VOF method. The level-set function F is a signed distance function where $F=0$ represents the interface, $F>0$ the liquid phase and $F<0$ the gas phase. It follows

$$\frac{\partial F}{\partial t} + (\mathbf{u} \cdot \nabla)F = -|\nabla F| s_L, \quad (5)$$

where s_L is the surface regression speed due to vaporisation. F is converted into the colour function ϕ , a Heaviside function of F . For example, the density is given by $\rho = (1-\phi)\rho_G + \phi\rho_L$ where ρ_L and ρ_G are the liquid and gas density, respectively.

The jump conditions due to phase change are given at the surface [39,40,45]. The heat balance at the liquid/gas surface gives

$$\begin{aligned} \Delta \dot{m}_v &= [I - \lambda \nabla T \cdot \mathbf{n} - \sigma \varepsilon (T^4 - T_0^4) - h(T - T_0)] \\ \dot{m}_v (Y_{i,G} - Y_{i,L}) &= [\rho D \nabla Y_i \cdot \mathbf{n}], \end{aligned} \quad (6)$$

where \dot{m}_v is the vaporisation rate, I is the laser intensity, h is the heat transfer coefficient, λ is the thermal conductivity and \mathbf{n} is the surface normal vector. The subscripts L and G represent the liquid and gas phase, respectively. The brackets denote the difference $[f] = f_L - f_G$. At the same time, the recoil pressure [22-24] works on the vaporising interface. For the mass fraction, the above constraint is given on the vaporising surface. The velocity satisfies [45]

$$\dot{m}_v = \rho_L (\mathbf{u}_S - \mathbf{u}_L) \cdot \mathbf{n} = \rho_G (\mathbf{u}_S - \mathbf{u}_G) \cdot \mathbf{n}. \quad (7)$$

where the surface velocity \mathbf{u}_S is the sum of the liquid velocity and the surface regression velocity, i.e. $\mathbf{u}_S = \mathbf{u}_L + \mathbf{s}_L$. The surface regression velocity is given as $\mathbf{s}_L = s_L \mathbf{n} = (\dot{m}_v / \rho_L) \mathbf{n}$. The density satisfies

$$\mathbf{u}_G - \mathbf{u}_L = -(\rho_G^{-1} - \rho_L^{-1}) \dot{m}_v \mathbf{n}.$$

(8)

The vapour mass fraction and the vapour pressure at the surface are given by the Clapeyron-Clausius relation. For a locally multi-component surface, mixture vaporisation is considered by Raoult's law.

The equation of state (EOS) for gas is given by the ideal-gas law, and the EOS for liquid is given by Tait's empirical formulation [39,40]

$$\frac{p + A_w}{p_0 + A_w} = \left(\frac{\rho}{\rho_0} \right)^{\gamma_w}, \quad (9)$$

where the subscript 0 denotes the reference state, and $A_w = 296.3 \text{ MPa}$ and $\gamma_w = 7.415$.

The temperature-dependent physical properties of metals are retrieved from databases and incorporated into the code to simulate AM problems. Details are described in the Appendix.

The advective term is discretized based on the CIP (Cubic Interpolated Pseudo-particle or Constrained Interpolation Profile) method [46], in which a third-order polynomial fitting is used for flow variables and their derivatives to assure the accuracy. The pressure is obtained by solving the pressure Poisson equation including the effect of the speed of sound. Other terms such as viscous term and heat conduction term are discretized using the central differencing.

The method proposed in this work has been developed based upon the multiphase flow algorithm [38-42]. Each phenomenon relevant to AM has been validated. Surface shape tracking by the CLSVOF method has been validated for droplet and spray problems where surface tension plays an important role [38-42]. Heat transfer, vaporisation and multi-species mixing have been validated in [41,47]. The thermo-capillary migration due to the Marangoni effect has been quantitatively validated and the role of Péclet number has been discussed [42]. The Stefan problem for liquid/gas phase transformation (boiling) has been quantitatively investigated with good agreement with the theory [40]. These validation cases indicate that the present numerical method can accurately capture the thermal-chemical-fluid flow dynamics in AM. For the phenomena more directly relevant to AM,

temperature distribution by laser heating [48] was compared and the present model showed good agreement. A validation example directly related to vaporisation in AM is shown here. Although currently experimental data on vapour mass loss are not well available, a recent experimental and modelling study of Zhang *et al.* [34] is referenced. The experiment was conducted for Ti-6Al-4V alloy, where the laser power was 330W, the scanning speed was 250mm/s and the laser spot diameter was 50 μ m. Figure 1a shows the ratio of the evaporative fluxes of Al and Ti with respect to the surface temperature [34], with the present result shown as circular dots. The trend of larger vaporisation for Al is in agreement. Figure 1b shows the calculated composition of the metal after being heated and evaporated. The experimental data [34] were obtained by an after-treatment destructive method using the inductively coupled plasma optical emission spectrometer (ICP-OES). Although the simulation data slightly overestimate the Al mass loss (smaller local Al composition), they are close to the experimental values. It can be emphasised that the trend of larger vapour mass loss of Al is reproduced in the present simulation and thus vaporisation is well predicted.

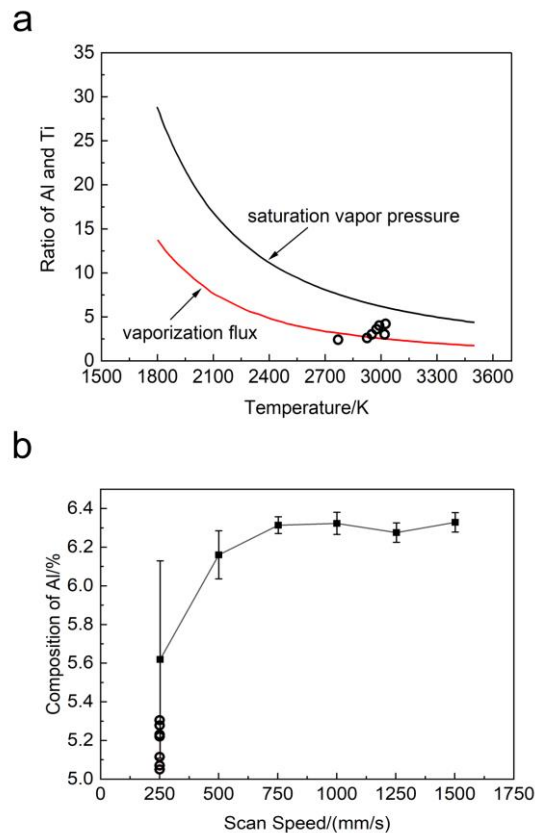


Fig. 1 Vaporisation characteristics of Ti-6Al-4V [34]. (a) Ratio of vaporisation mass flux and (b) composition of Al after vaporisation. The original figures are Fig. 3b and Fig. 5 of

Ref. [34] and reproduced by digitisation. The numerical results at different simulation times are plotted as circular dots.

Still, as this case exemplifies, exact quantitative analysis by experiments is difficult, but future efforts must be pursued for better characterisation in combination with numerical simulation [1,49]. Currently, to set a future AM research direction, several methods are sought for increasing sophistication in *in-situ* characterisation such as *in-situ* chemical imaging/photography using X-ray synchrotron measurement or post-mortem analysis using mass spectroscopy, inductively coupled plasma-optical emission spectroscopy (ICP-OES), electron probe micro analyser (EPMA), or energy dispersive X-ray spectroscopy (EDS) [1,50]. It is expected that more thorough comparison will be possible in the near future.

2.2. Case Setup

2.2.1 Elemental AM

21 elements studied in this paper are shown in Fig. 2. Transition metals relevant to superalloys (shown in the enlarged area in the figure) are investigated in each case of pure element AM. Powder size distribution is given by a dataset which mimics realistic powder settings. The cumulative median diameter is $14\mu\text{m}$ and the maximum powder diameter is $36\mu\text{m}$. The grid resolution is $4\mu\text{m}$. The initial metal/air temperature is set at 300K. Since it is impossible to investigate all the effects of laser parameters, the laser parameters are basically fixed in the present study. The laser power is set as $Q_L=400\text{W}$, $z_e-z_i=128\mu\text{m}$, $r_e=36\mu\text{m}$ (spot diameter of $72\mu\text{m}$) and $r_i=8\mu\text{m}$ for Eq. (4). The absorptivity [51], as a local physical property value, is $\eta_L=0.3$. The laser sweep speed is 1000mm/s .

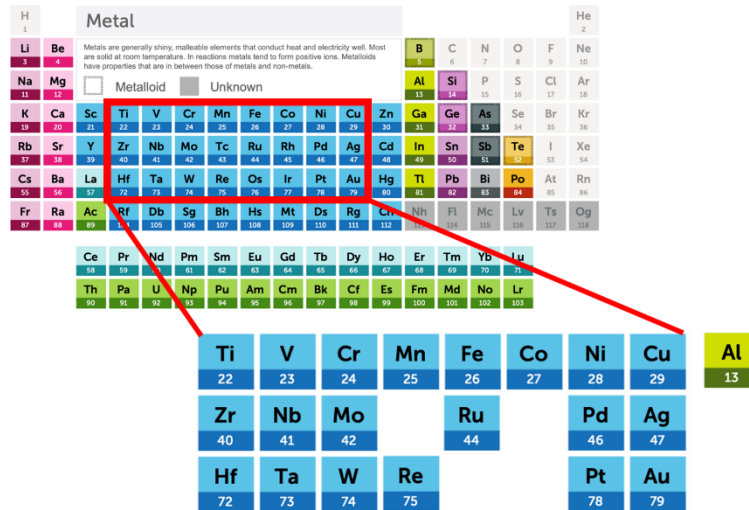


Fig. 2 Transition metal elements investigated in this study.

2.2.2 *In-situ* binary AM

Three combinations of binary alloys are investigated: NiAl: basis for multi-component superalloys, NiTi (Nitinol): shape memory alloy and TiAl (Titanium aluminide): light weight alloy. The spatial powder distribution is set the same as in the elemental AM cases. To see mixing clearly, the substrate is composed of one pure element denoted by the first element symbol. For example, for NiAl, the substrate is composed of Ni, on which powders of two elements (Ni and Al) are randomly placed as shown later in Fig. 4a. The laser parameters are set the same as in the elemental AM cases. The laser heat absorption coefficient [51] is set at 0.3 and 0.6 to see the effects of flow process parameter.

3. Results and discussion

3.1. Melt flow dynamics

Figure 3a,b shows the schematic representation of the relevant phenomena in AM. During the melting process, the thermal-fluid flow of melted metal exhibits formation of a keyhole, flow circulation and pore formation in the melt pool. Mass loss is induced by periodic vapour jet ejection. The vapour jets induce mixing with the ambient air as well, leading to a consideration of spatter generation and possible surface layer oxidation due to surface-air reaction. In *in-situ* alloying, liquid metal mixing also occurs simultaneously with melting and the mass loss is either caused by isolated

local vaporisation of each exposed element when multi-metal mixing is still not sufficient, or by preferential vaporisation after liquid metal mixing proceeds. Fig. 3c shows a typical bird's view of heated powder bed of Ni at $t=60\mu\text{s}$. Laser is scanned in the x -direction and the high-temperature region moves along with the laser motion. In the high-temperature region, molten metal flow is induced both near the surface and deep inside, occasionally accompanied by spatter ejection. The molten flow dynamics observed here is reasonably the same as experimental and computational observations [17,18,22-24] and multi-species vaporisation is included and discussed hereafter.

The thermal conductivity and kinematic viscosity at melting point for each element are shown in Fig. 3d with the bubble size corresponding to the liquid density. The thermal diffusivity is a measure of the speed of heat spread, and the kinematic viscosity is a measure for the velocity spread (induced motion), which leads to different thermal-fluid flow and vapour characteristics among elements. In Fig. 3e-j, six representative elements significant for alloys are chosen to see the molten metal flow inside. In the direction from Fig. 3e to j, the thermal diffusivity is larger, which means that the given heat spreads faster. In all the cases, the overall dynamics is similar to the schematic picture in Fig. 3a. In the left-hand-side part of the melt pool (the front side of laser scanning), the molten liquid flows downward due to the recoil motion, forming a keyhole. Then, the flow circulates upward in the right-hand-side of the keyhole, inducing secondary circulation.

The smaller thermal diffusivity of Fe, Ti and Ni makes a steep temperature gradient in the front region (Fig. 3e,f,g). While the heat spreads slowly, the induced velocity is larger due to the larger kinematic viscosity (later discussed), which results in fragmented liquid/solid boundary and pores/spatter are sometimes formed (Fig. 3f,h) or temporary bridge formation (Fig. 3g) can be seen. Au, with its high thermal conductivity, the heat spreads broader. The mass loss is larger (later discussed) and due to the recoil pressure, the induced velocity is not small and the keyhole is deeper. The observed liquid flow dynamics is highly unsteady and different from element to element, which can be captured by high-fidelity numerical simulation.

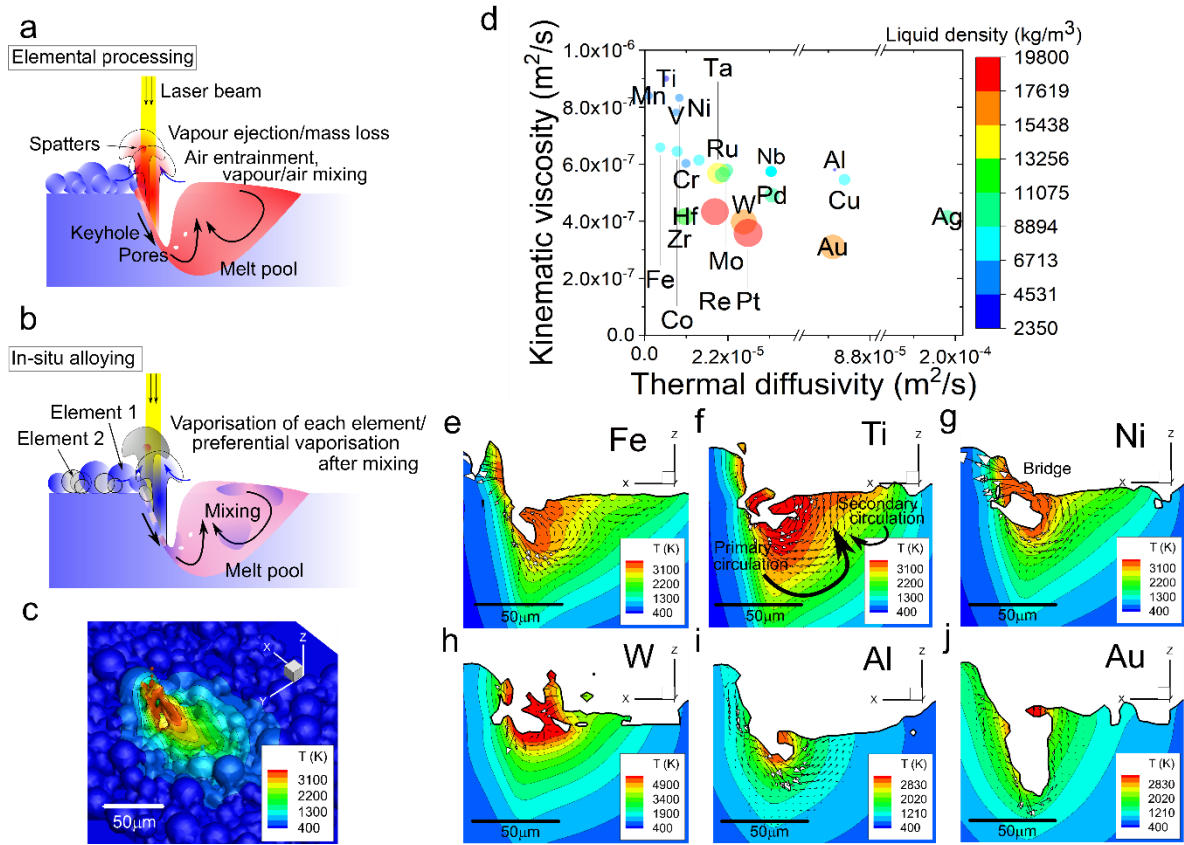


Fig. 3 (a,b) Schematic of relevant phenomena for elemental AM and *in-situ* alloying.

During the melting process, the thermal fluid flow of melted metal exhibits formation of a keyhole, flow circulation and pores in the melt pool. In *in-situ* alloying, liquid mixing also occurs. Mass loss is induced by periodic vapour jet ejection. For binary alloys, the mass loss is either caused by local vaporisation of each exposed element or by preferential vaporisation after liquid mixing. (c) Bird's view of melted Ni at $t=60\mu\text{s}$. (d) Thermal diffusivity and kinematic viscosity of each element. (e-j) Instantaneous snapshots of temperature and velocity fields in the melt pool at $t=60\mu\text{s}$.

In *in-situ* alloying, liquid mixing adds more complexity to the flow and metal vaporisation dynamics (later discussed), which will have a large impact on the final composition. Figure 4a,b shows the bird's view of the NiAl case. It is clear that the initially separated Ni and Al are mixed after being melted by laser. Inside, the keyhole and the melt pool are formed similarly as in the pure element cases (Fig. 3c).

Figure 4d-f compares the mixing inside. Overall, for all the cases, a mixture of two components is formed in the melt pool. The streamline analysis in Fig. 4d shows that on the central plane, the downward flow in the front of the keyhole and primary/secondary circulations in the melt pool enhance species mixing, as indicated by the dashed yellow arrows. The 3D circular flow toward the side is also formed, as indicated by the solid red arrows, which also carries species for mixing. This flow pattern is very similar to recently-reported synchrotron images [14,15]. In the front part of the keyhole, the powders are composed of a pure element and melting occurs reciprocally for each element. Mixing initiates here but does not progress very much due to the lack of mixing time. The larger circular flow in the melt pool contributes more to convective mixing due to a longer time scale. Similar mixing behaviour can be observed for NiTi (Fig. 4e) and TiAl (Fig. 4f). The mixture size is the largest for TiAl, since Ti has a larger kinematic viscosity and as a solvent, compared to Ni, a larger flow motion is generated. In addition, the effect of the thermal diffusivity also exists. Since Al has a larger thermal diffusivity, heat spread/melting of Al is always faster.

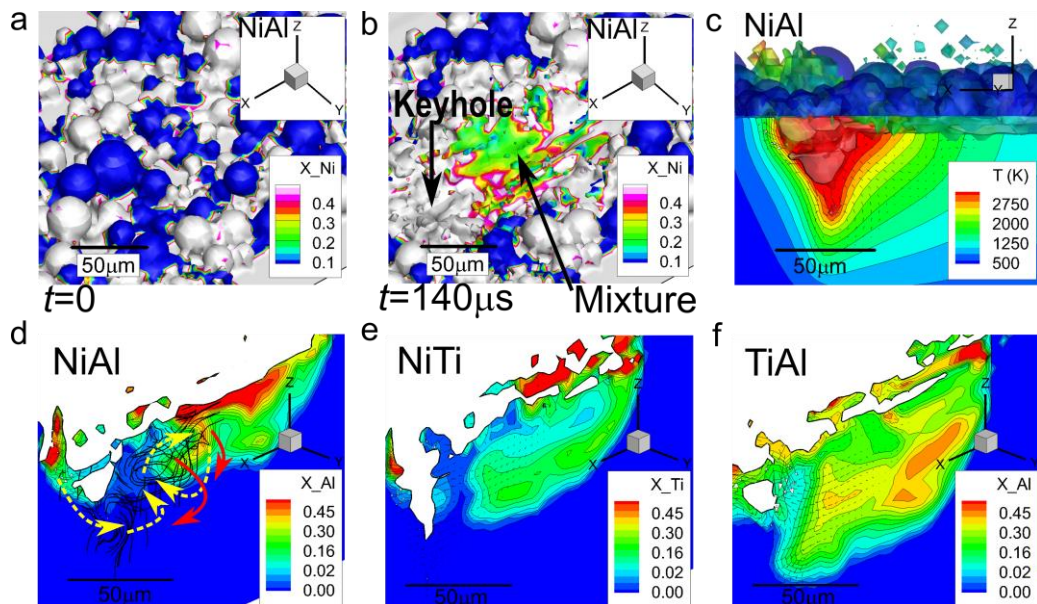


Fig. 4 Behaviour of binary *in-situ* alloying. (a,b) Mixture formation on the surface of NiAl. Initially at $t=0$, white indicates Ni and blue indicates Al. (c) Keyhole and melt pool formation inside the substrate at $t=140\mu\text{s}$ (NiAl). (d) Inside view of melt pool molar composition in terms of Al molar fraction. The dashed yellow arrows indicate flow

motion on the central plane, and the solid red arrows show 3D circular motion. (e,f)

Molar fraction of Ti and Al for NiTi and TiAl, respectively.

3.2. Chemistry-process parameters

The chemistry-process parameters of Reynolds (Re) and Péclet (Pe) numbers are important for thermal fluid flows. Re is defined as $Re=UL/\nu$, where ν is the kinematic viscosity, and represents the ratio of the flow inertia to the viscous force. Here, L is taken as the melt pool size in the laser scanning direction and U is the maximum velocity magnitude of the liquid metal flow (Fig. 5a). Pe is defined as $Pe=UL/\alpha$, where α is the thermal diffusivity, and represents the ratio of convective heat transfer to diffusive heat conduction.

Figure 5b-d shows the relationships between Re and Pe , and the keyhole depth, the liquid velocity and the melt pool size. The bubble symbol size (=molar loss rate) will be discussed later in detail. The induced liquid velocity is physically affected by the kinematic viscosity, and the trend of the kinematic viscosity in Fig. 3d can be basically seen in Fig. 5. Generally, elements with larger molar loss, such as Mn, Fe, Ni and Au, exhibit relatively larger melt pool and larger liquid velocity, resulting in larger Re . Meanwhile, elements with smaller molar loss, such as Cu, Mo and Ta, show relatively smaller pool size or smaller velocity magnitude. This suggests that the molar loss is larger when Re is larger. This dependence is made clear in Fig. 6. Overall, the dependence of liquid velocity and key hole size on Pe is not as strong as Re but the melt pool size is dependent on both parameters. This indicates that Re and Pe link between the composition and process.

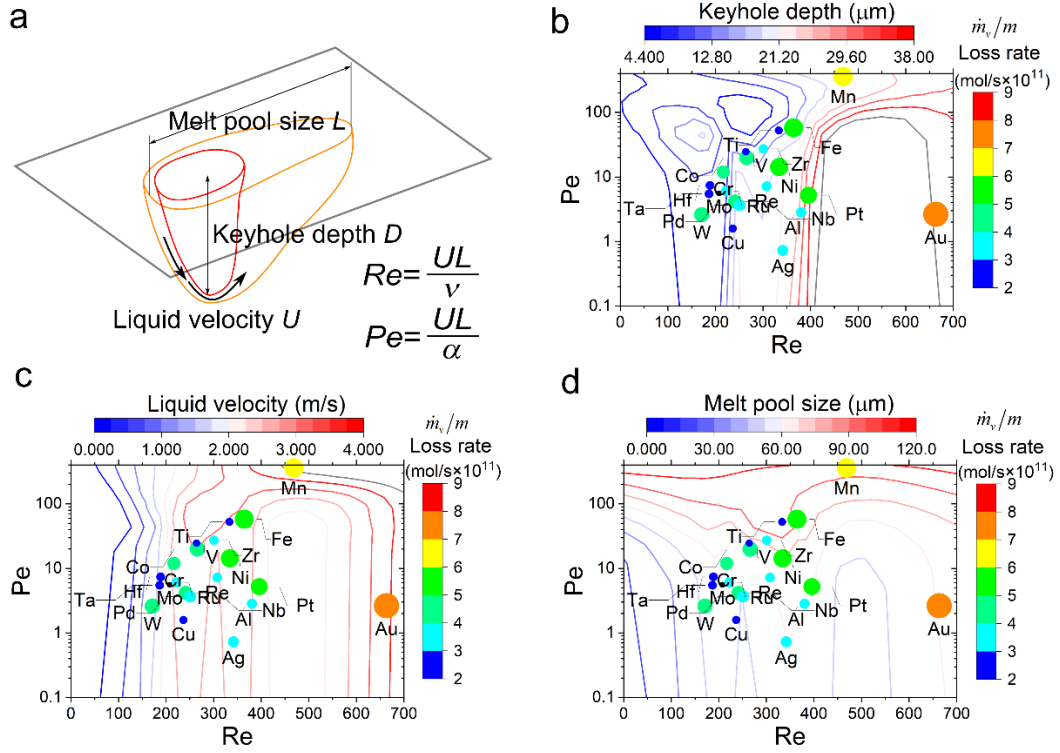


Fig. 5 The effect of Re and Pe . (a) Schematic and definition. (b) Keyhole depth, (c) liquid velocity and (d) melt pool size.

3.3. Mass loss characteristics

The mass loss during AM is significantly important since it is strongly related to the final product quality in alloys, such as local composition, microstructures and mechanical strength. Figure 6a shows the mean mass loss rate against the rough estimation from the Hertz-Knudsen relation at boiling point $\dot{m}_v = \sqrt{m/2\pi k T_b} p_v \sim \sqrt{m/T_b}$, where m is the atomic mass, T_b is the boiling temperature and p_v is the vapour pressure [52]. Heavy elements, such as refractory metals (W, Hf, Ta) and precious metals (Au, Pt), exhibit larger mass loss. Elements with medium densities (Mo, Ru, Nb) show medium mass loss rates. Elements with relatively lighter densities (Ti, Al) are in the lower mass loss range. Overall, they are correlated with the estimate. In the estimate, however, the fluid dynamic effects are not considered and discussed next.

Figure 6b shows the mass loss rate normalised by the atomic weight. The elements are grouped according to the atomic weight (3d, 4d and 5d in the periodic table) and the rates of the three groups

become similar. The rate may be different by heating conditions, but it is important for prediction to know that there is some similar range where different classes of elements reside.

Figure 6c,d highlights the link between the mass loss and Re and Pe . The dependence on Re is clear. The mass loss is increased as $\sim \ln(Re)$, and the three groups are on the same correlation. The dependence on Pe is less clear and the data points are more scattered, but the weak trend of increased loss rate as $\sim \ln(Pe)$ can be also seen. Thus, it is indicated that the fluid dynamic effect is more dominant in determining the mass loss rate.

For the binary alloys, vaporisation is mostly dominated by the preferential vaporisation of the mixture except at the very beginning. Since the local temperature is common for the components, a volatile element with a lower boiling point temperature and a lower latent heat tends to vaporise faster, as indicated in Fig. 6e. For example, Al tends to vaporise earlier due to lower boiling temperature. More Ni vaporisation is observed than Ti for NiTi. This is, however, not simply understood by the physical properties only, since local mixing needs to be enhanced by the fluid dynamic motion. Re in the solvent melt pool in Fig. 6e indicates slightly more mixing in TiAl with a larger Re , which coincides with the visualised results in Fig. 4d-f. And the laser parameter ($\eta=0.3$ and 0.6 in this case) causes the variation of Re . Therefore, for *in-situ* alloying, the fluid dynamic effect needs to be considered as well as properties of each element.

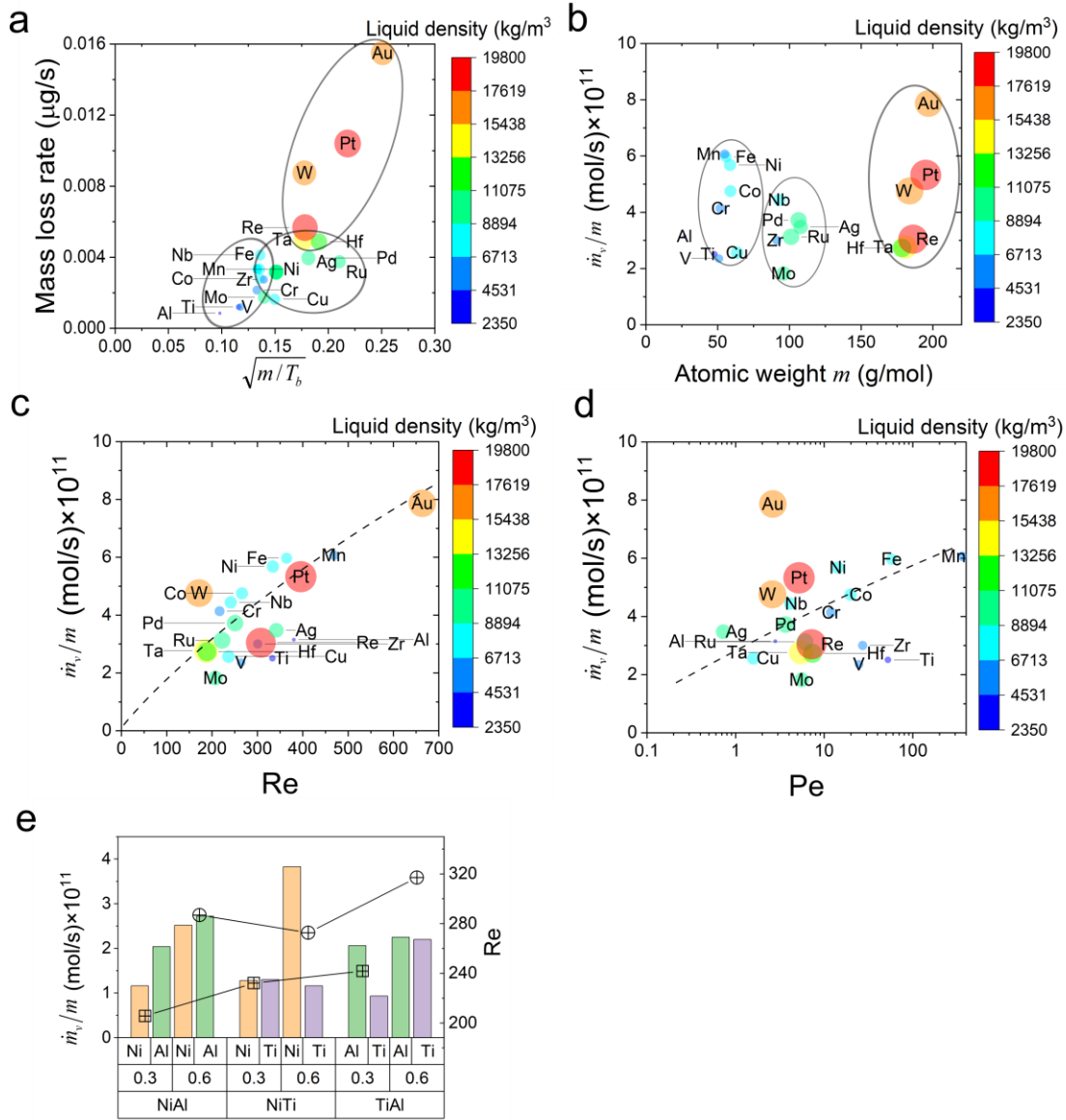


Fig. 6 (a) Mass loss rate plotted against the estimate. (b) Mass loss rate normalised by the atomic weight plotted against the atomic weight. (c,d) Dependence of mass loss rate on Re and Pe . The bubble size indicates the liquid-phase density. (e) Mass loss rate of components (indicated by bars) and Re (indicated by symbols) in *in-situ* binary alloying. 0.3 and 0.6 mean the laser heat absorptivity tested in this study.

3.4. Vapour mixing dynamics with vortex generation

In order to identify the vapour dynamics, cases of Ti are used with different laser powers. Compared to the baseline laser spot size of $r_e=36\mu\text{m}$ (spot diameter of $72\mu\text{m}$), an additional case of $r_e=70\mu\text{m}$

(spot diameter of $144\mu\text{m}$) is conducted here. Figure 7 shows the results. For the smaller laser spot diameter (Fig. 7a), a keyhole is formed, similarly as in the cases in Fig. 3. The vapour is generally ejected normal to the melted surface and in this case in the upper right ($-x+z$) direction. Here, an iso-surface of $T=2500\text{K}$ in the gas phase is drawn. For the larger laser spot case, the conduction mode appears without a distinct keyhole (Fig. 7b). The melted surface is rather flat due to the smaller temperature gradient and the vapour plume ejection direction is mostly upright in the $+z$ direction.

The ejected vapour mixes with the ambient air. The scalar dissipation rate (SDR) $\chi = D|\nabla Z|^2$ represents the inverse of the mixing time scale $\tau_{mix} \sim \chi^{-1}$, where the mixture fraction Z is the vapour mass fraction here ($Z=Y_v$). Typically, the front and periphery regions of a jet are where the SDR is large and intense mixing occurs. The colour on the $T=2500\text{K}$ iso-surface represents the SDR in the natural log scale. The jet front and the root regions can be observed as high SDR regions, where mixing between the metal vapour and the ambient gas occurs. A larger metal powder needs to be heated longer than a smaller powder due to the difference in the volume-to-surface ratio. Therefore, small short-duration jets are locally made along the laser scanning direction where the powder size variation exists, and the vapour ejection is highly unsteady and intermittent. The black ring-like structure in Fig. 7 indicates the iso-surface of the magnitude of the vorticity $\omega = \nabla \times \mathbf{u}$. It is clear that the ejected vapour creates a gaseous vortical structure at the jet root, which strongly entrains the ambient air into the vapour gas. For both the keyhole and conduction modes, this motion is basically the same except the slight difference in the inclination angle of jet ejection. Due to the entrained air, the melted surface is exposed to the oxygen stream and thus surface oxidation is an important issue in AM regarding the final product quality. Although the present simulation does not include surface oxidation reactions, it is an interesting issue to be investigated in the future. The overall vapour ejection characteristics have been also experimentally observed [10] and are overall the same. The simulated results here add more information on the detailed vapour vortical structures.

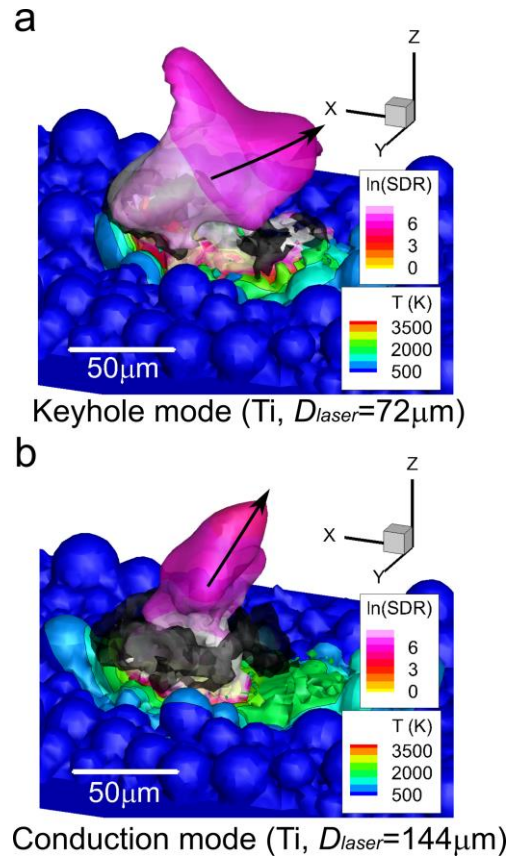


Fig. 7 Vapour ejection, air entrainment and mixing for Ti. (a) is for the laser spot diameter of $72\mu\text{m}$ (keyhole mode) and (b) for $144\mu\text{m}$ (conduction mode). The SDR is shown on the iso-surface of vapour of $T=2500\text{K}$. The black iso-surface represents the vorticity iso-surface.

4. Conclusions

Using the multi-species multi-phase thermal fluid flow simulation method, very complicated AM processes have been elucidated including the fluid flow dynamics and mass loss characteristics due to metal vaporisation. The following key findings have been obtained.

1. Formation of the melt pool, keyhole and flow for each element has been captured by the present simulation method. The behaviour is determined by the two process parameters of Re and Pe , where the physical properties of thermal diffusivity and kinematic viscosity play a role. The dependence of melt pool liquid velocity and key hole size on Pe is not as strong as on Re , but the melt pool size is dependent on both parameters. When the loss by vaporisation is larger, Re

is larger. These element-by-element differences indicate that Re and Pe link between the composition and process.

2. The mass loss rate for each element is more dependent on Re , with the correlation of mass loss as $\sim \ln(Re)$. The dependence on Pe is less clear, but the weak trend of increased mass loss rate as $\sim \ln(Pe)$ is also observed. Therefore, the fluid flow process strongly determines the mass loss rate.
3. In the *in-situ* alloying for binary alloys, after the melting of each pure-element powder, metal liquid mixing is enhanced due to the circular flow motion in the melt pool and the composition of elements varies locally. Similarly, as in the pure element cases, the melt pool size and the magnitude of the flow motion are determined by the physical properties of thermal diffusivity and kinematic viscosity, and thus by the chemistry-process parameters of Re and Pe . The trend of vaporisation loss of each component can be predicted by thermal-chemical-fluid flow simulation, and it is suggested that the mass loss can be again depicted by the dynamic process characterised more strongly by Re . Therefore, the fluid dynamic effect, as well as the properties of each element, is a significant factor that determines the mass loss characteristics.
4. The vapour ejection dynamics is tracked in the gas phase. The ejection direction is determined by the dynamic shape of the melt pool and the keyhole. Due to the ejected vapour jet, entrainment of the surrounding gas is induced with strong mixing with the vapour. Such a gas motion may affect surface oxidation, and further investigation is needed in the next step.
5. Above all, high-fidelity simulation can be a powerful tool to predict complicated thermal-solutal-fluid flow in AM and the present study highlights the significance of digital materials design, which will advance an understanding for further applications of AM in industries.

Appendix

A. Physical properties of each element

The physical properties such as solid/liquid densities, melting temperature, boiling temperature, heat capacity, latent heat, thermal conductivity, surface tension, viscosity and diffusion coefficients are retrieved from databases and experimental works in the literature [53-68].

For the heat capacity, open source databases [53,54] are utilised to construct the temperature dependent table for heat capacity as shown in Fig. A.1. In the code, the data are included as curve-fit polynomials. In the liquid phase, the temperature dependence is very small. In the vapour phase, the temperature dependence is neglected for simplicity. Data are not completely available, especially in the high temperature region, for Ru, Pd, Ag, Re, Pt and Au. The high temperature values are extrapolated from a lower value.

Figure A.1 also shows the thermal conductivity. It is more difficult to obtain the thermal conductivity data in a wide range of temperature, compared to the heat capacity [53,54]. Therefore, values for the low temperature region and for the molten metal are used to interpolate the values in the middle. Cu, Al, Ag and Au have much larger thermal conductivity than other elements. In the code, the data are included as curve-fit polynomials.

For the atomic weight, solid density, liquid density, melting temperature, boiling temperature, latent heat of melting and latent heat of boiling, constant values are used as shown in Table A.1.

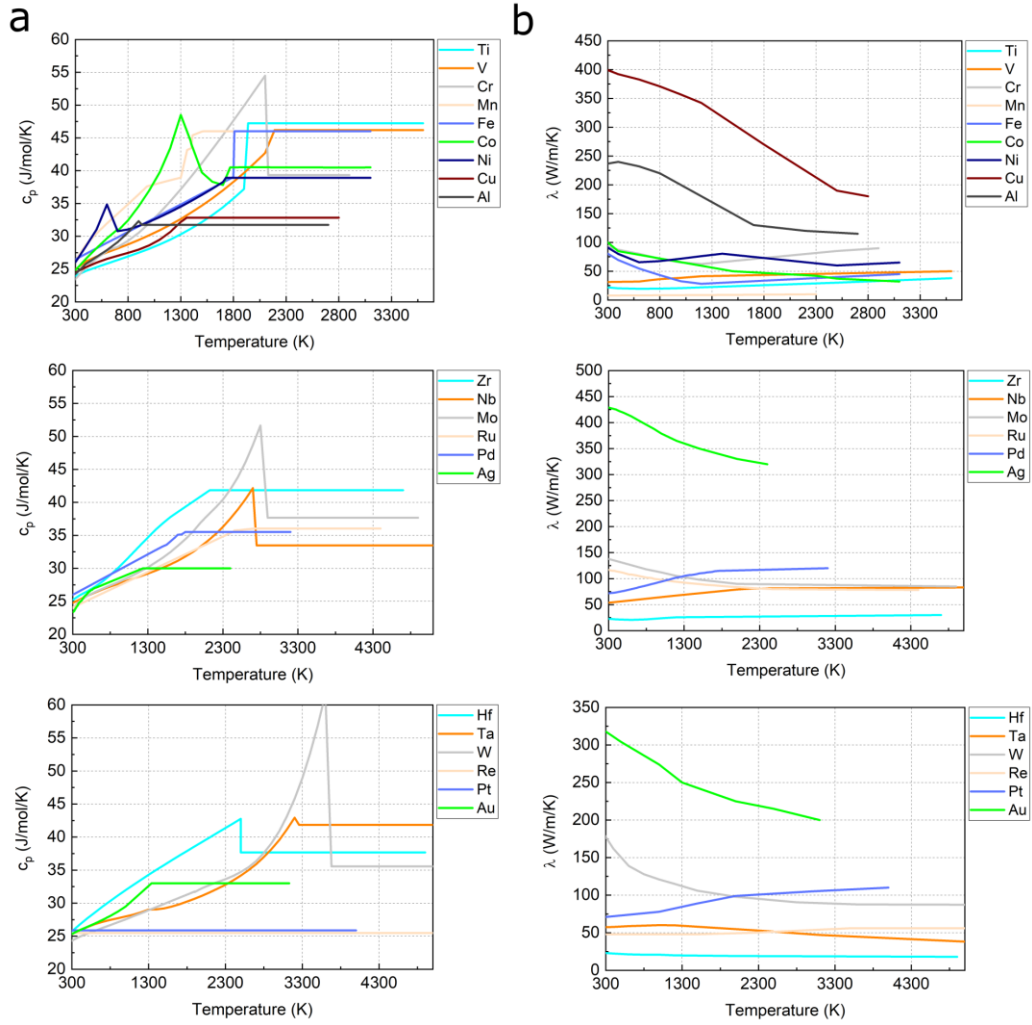


Fig. A.1 Heat capacity (J/mol/K) and (b) thermal conductivity (W/m/K).

Surface tension data are available from levitation experiments [55-67]. The general formula for the surface tension coefficient of a molten metal is

$$\sigma(T) = \sigma_0 + \frac{d\sigma}{dT}(T - T_{melt}) \quad (10)$$

where T_{melt} is the melting temperature. Table A.2 gives the values for each element.

The viscosity data are available from the open database [54] and the experiments [55-67]. Table A.3 summarises the formulations. These fitted formulations are for the range near the melting point. In the higher temperature liquid beyond the range, the viscosity value at the high-limit temperature of the recommended range is extrapolated.

The binary diffusion coefficients in liquid metals are very difficult to estimate, and a typical value of $D=1.0 \times 10^{-8} \text{ m}^2/\text{s}$ is used [68].

Table A.1 Physical properties of elements.

Element	Atomic weight (g/mol)	Solid density (kg/m ³)	Liquid density (kg/m ³)	Melting temperature (K)	Boiling temperature (K)	Δh_{melt} (kJ/mol)	Δh_{boil} (kJ/mol)
Ti	47.87	4506	4110	1941	3560	14.2	425
V	50.94	6000	5500	2183	3680	21.5	459
Cr	52.00	7190	6300	2180	2944	21.0	340
Mn	54.94	7210	5950	1519	2334	12.9	221
Fe	55.85	7874	6980	1811	3134	13.8	340
Co	58.93	8900	7750	1768	3200	16.1	377
Ni	58.69	8908	7810	1728	3186	17.5	378
Zr	91.22	6520	5800	2128	4682	14.0	573
Nb	92.91	8570	7830	2741	5015	30.0	690
Mo	95.96	10280	9330	2896	4912	37.5	598
Ru	101.07	12450	10650	2607	4423	38.6	592
Hf	178.49	13310	12000	2506	4876	27.2	571
Ta	180.95	16654	15000	3258	5783	36.6	733
W	183.84	19250	17600	3695	5828	35.3	807
Re	186.21	21020	18900	3459	5869	60.4	704
Al	26.98	2700	2375	934	2792	10.7	294
Cu	63.55	8940	8020	1358	2835	13.3	300
Pd	106.42	12023	10380	1828	3236	16.7	362
Ag	107.87	10490	9320	1235	2435	11.3	251
Pt	195.08	21450	19770	2041	4098	22.2	469
Au	196.97	19320	17310	1337	3129	12.6	324

Table A.2 Values for surface tension.

Element	σ_0 (mN/m)	$\frac{d\sigma}{dT}$ (mN/m/K)
Ti	1557	-0.156
V	1935	-0.27
Cr	1642	-0.20
Mn	1152	-0.35
Fe	1862	-0.39
Co	1881	-0.34
Ni	1796	-0.35
Zr	1512	-0.37
Nb	1937	-0.199
Mo	2290	-0.26
Ru	2258	-0.24
Hf	1620	-0.1
Ta	2150	-0.21
W	2480	-0.31
Re	2710	-0.23
Al	871	-0.155
Cu	1330	-0.23
Pd	1482	-0.279

Ag	925	-0.21
Pt	1746	-0.307
Au	1145	-0.20

Table A.3 Formula for viscosity ($R=8.314$ J/mol/K)

Element	μ (mPa·s)
Ti	$\mu(T) = 4.42 - 6.67 \times 10^{-3}(T - T_{melt})$
V	$\mu(T) = 1.23\exp(2.27 \times 10^4/RT)$
Cr	$\mu(T) = 1.7 \times 10^{-4}\exp(185 \times 10^3/RT)$
Mn	$\mu(T) = 0.12\exp(20 \times 10^3/RT)$
Fe	$\mu(T) = 0.2388\exp(47.44 \times 10^3/RT)$
Co	$\mu(T) = 0.2042\exp(48.13 \times 10^3/RT)$
Ni	$\mu(T) = 0.3155\exp(38.85 \times 10^3/RT)$
Zr	$\mu(T) = 4.83 - 5.31 \times 10^{-3}(T - T_{melt})$
Nb	$\mu(T) = 4.50 - 5.62 \times 10^{-3}(T - T_{melt})$
Mo	$\mu(T) = 0.27\exp(73 \times 10^3/RT)$
Ru	$\mu(T) = 20.53 - 5.52 \times 10^{-3}T$
Hf	$\mu(T) = 178.36 - 5.24 \times 10^{-3}T$
Ta	$\mu(T) = 0.0035\exp(213.3 \times 10^3/RT)$
W	$\mu(T) = 0.11\exp(12.8 \times 10^4/RT)$
Re	$\mu(T) = 0.08\exp(1.33 \times 10^5/RT)$
Al	$\mu(T) = 0.2565\exp(13.08 \times 10^3/RT)$
Cu	$\mu(T) = 0.5287\exp(23.85 \times 10^3/RT)$
Pd	$\mu(T) = 4.22$
Ag	$\mu(T) = 0.453\exp(22.2 \times 10^3/RT)$
Pt	$\mu(T) = 20.0 - 7.36 \times 10^{-3}T$
Au	$\mu(T) = 1.099\exp(17.62 \times 10^3/RT)$

B. Influence of energy reflection during laser selective melting: Ray tracing

Although the heat model of Xu *et al.* [43] has been known to well predict the heat distribution in AM, the laser heat is, in principle, carried by the laser light and heating initiates from the exposed surface. Here, the ray tracing technique [7,69,70] is tested to compare with the heat model. The laser parameters are set the same as those of Fig. 3. Multiple reflections are considered and the energy is deposited at the surface at each reflection with the absorption coefficient of 0.6.

Figure B.1 shows the temperature distribution for Ni at $t=53$ and $55\mu\text{s}$. The laser rays undergo multiple reflections inside the keyhole. Compared with the heat model [43] where the heat is averagely distributed, local surface inclination determines the temperature rise and the direction of reflected rays. Therefore, local variance tends to induce additionally small and faster fluctuations in keyhole shape, as seen in the figure. But overall, surface melting and keyhole/melt pool formation are

similarly reproduced and the present method with Xu *et al.*'s heat model [43] is well effective and efficient in AM simulation.

Trapp *et al.* [51] and Khairallah *et al.* [7] investigated the melt flow dynamics and reported the effect of the variation in the surface heat absorptivity in accordance with the laser scanning speed and power. Such an issue is one of the future topics to be investigated.

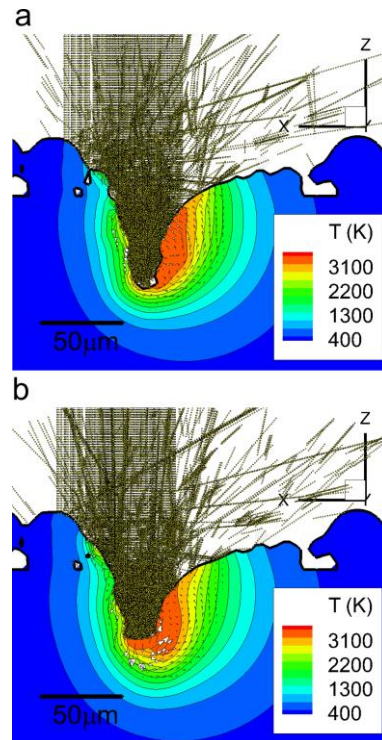


Fig. B.1 Temperature distribution for Ni at (a) $t=53\mu\text{s}$ and (b) $t=55\mu\text{s}$. The brown loci indicate the photon paths on this plane.

Acknowledgements

This work was supported by Next Generation TATARA Project sponsored by the Government of Japan and Shimane Prefecture. Part of simulation was conducted on Kyushu University supercomputer system ITO. Chinnapat Panwisawas would like to acknowledge the funding from Innovation Fellowship by Engineering and Physical Science Research Council (EPSRC), UK Research and Innovation (UKRI), under the grant number: EP/S000828/2.

References

- [1] T. DebRoy, H.L. Wei, J.S. Zuback, T. Mukherjee, J.W. Elmer, J.O. Milewski, A.M. Beese, A. Wilson-Heid, A. De, W. Zhang, Additive manufacturing of metallic components – Process, structure and properties, *Prog. Mater. Sci.* 92 (2018) 112-224.
<https://doi.org/10.1016/j.pmatsci.2017.10.001>
- [2] R.C. Reed, *The Superalloys: Fundamentals and Applications*, Cambridge University Press 2008.
- [3] T.M. Pollock, Alloy design for aircraft engines, *Nat. Mater.* 15 (2016) 809-815.
<https://doi.org/10.1038/nmat4709>
- [4] J.B. Roca, P. Vaishnav, E.R.H. Fuchs, M.G. Morgan, Policy needed for additive manufacturing, *Nat. Mater.* 15 (2016) 815-818. <https://doi.org/10.1038/nmat4658>
- [5] C. Panwisawas, Y.T. Tang, R.C. Reed, Metal 3D printing as a disruptive technology for superalloys, *Nat. Commun.* 11 (2020) 2327. <https://doi.org/10.1038/s41467-020-16188-7>
- [6] A.T. Polonsky, T.M. Pollock, Closing the science gap in 3D metal printing, *Science* 368 (2020) 583-584. <https://doi.org/10.1126/science.abb4938>
- [7] S.A. Khairallah, A.A. Martin, J.R.I. Lee, G. Guss, N.P. Calta, J.A. Hammons, M.H. Nielsen, K. Chaput, E. Schwalbach, M.N. Shah, M.G. Chapman, T.M. Willey, A.M. Rubenchik, A.T. Anderson, Y.M. Wang, M.J. Matthews, W.E. King, Controlling interdependent meso-nanosecond dynamics and defect generation in metal 3D printing, *Science* 368 (2020) 660-665.
<https://doi.org/10.1126/science.aay7830>
- [8] C. Zhao, K. Fezzaa, R.W. Cunningham, H. Wen, F. De Carlo, L. Chen, A.D. Rollett, T. Sun, Real-time monitoring of laser powder bed fusion process using high-speed X-ray imaging and diffraction, *Sci. Rep.* 7 (2017) 3602. <https://doi.org/10.1038/s41598-017-03761-2>
- [9] S. Ly, A.M. Rubenchik, S.A. Khairallah, G. Guss, M.J. Matthews, Metal vapor micro-jet controls material redistribution in laser powder bed fusion additive manufacturing, *Sci. Rep.* 7 (2017) 4085. <https://doi.org/10.1038/s41598-017-04237-z>
- [10] P. Bidare, I. Bitharas, R.M. Ward, M.M. Attallah, A.J. Moore, Fluid and particle dynamics in laser powder bed fusion, *Acta Mater.* 142 (2018) 107-120.
<https://doi.org/10.1016/j.actamat.2017.09.051>
- [11] L. Aucott, H. Dong, W. Mirihanage, R. Atwood, A. Kidess, S. Gao, S. Wen, J. Marsden, S. Feng,

- M. Tong, T. Connolley, M. Drakopoulos, C.R. Kleijn, I.M. Richardson, D.J. Browne, R.H. Mathiesen, H.V. Atkinson, Revealing internal flow behaviour in arc welding and additive manufacturing of metals, *Nat. Commun.* 9 (2018) 5414. <https://doi.org/10.1038/s41467-018-07900-9>
- [12] A.A. Martin, N.P. Calta, S.A. Khairallah, J. Wang, P.J. Depond, A.Y. Fong, V. Thampy, G.M. Guss, A.M. Kiss, K.H. Stone, C.J. Tassone, J.N. Weker, M.F. Toney, T. van Buuren, M.J. Matthews, Dynamics of pore formation during laser powder bed fusion additive manufacturing, *Nat. Commun.* 10 (2019) 1987. <https://doi.org/10.1038/s41467-019-10009-2>
- [13] S.M.H. Hojjatzadeh, N.D. Parab, W. Yan, Q. Guo, L. Xiong, C. Zhao, M. Qu, L.I. Escano, X. Xiao, K. Fezzaa, W. Everhart, T. Sun, L. Chen, Pore elimination mechanisms during 3D printing of metals, *Nat. Commun.* 10 (2019) 3088. <https://doi.org/10.1038/s41467-019-10973-9>
- [14] Q. Guo, C. Zhao, M. Qu, L. Xiong, S.M.H. Hojjatzadeh, L.I. Escano, N.D. Parab, K. Fezzaa, T. Sun, L. Chen, In-situ full-field mapping of melt flow dynamics in laser metal additive manufacturing, *Addit. Manuf.* 31 (2020) 100939. <https://doi.org/10.1016/j.addma.2019.100939>
- [15] S.J. Clark, C.L.A. Leung, Y. Chen, L. Sinclair, S. Marussi, P.D. Lee, Capturing Marangoni flow via synchrotron imaging of selective laser melting, *IOP Conf. Ser.: Mater. Sci. Eng.* 861 (2020) 012010. <https://doi.org/10.1088/1757-899X/861/1/012010>
- [16] V. Manvatkar, A. De, T. DebRoy, Spatial variation of melt pool geometry, peak temperature and solidification parameters during laser assisted additive manufacturing process, *Mater. Sci. Technol.* 31 (2015) 924-930. <https://doi.org/10.1179/1743284714Y.0000000701>
- [17] C. Qiu, C. Panwisawas, M. Ward, H.C. Basoalto, J. W. Brooks, M.M. Attallah, On the role of melt flow into the surface structure and porosity development during selective laser melting, *Acta Mater.* 96 (2015) 72-79. <http://dx.doi.org/10.1016/j.actamat.2015.06.004>
- [18] C. Panwisawas, C.L. Qiu, Y. Sovani, J.W. Brooks, M.M. Attallah, H.C. Basoalto, On the role of thermal fluid dynamics into the evolution of porosity during selective laser melting, *Scr. Mater.* 105 (2015) 14-17. <http://dx.doi.org/10.1016/j.scriptamat.2015.04.016>
- [19] M.J. Matthews, G. Guss, S.A. Khairallah, A.M. Rubenchik, P.J. Depond, W.E. King, Denudation of metal powder layers in laser powder bed fusion processes, *Acta Mater.* 114 (2016) 33-42.

- <http://dx.doi.org/10.1016/j.actamat.2016.05.017>
- [20] S.A. Khairallah, A.T. Anderson, A. Rubenchik, W.E. King, Laser powder-bed fusion additive manufacturing: Physics of complex melt flow and formation mechanisms of pores, spatter, and denudation zones, *Acta Mater.* 108 (2016) 36-45. <http://dx.doi.org/10.1016/j.actamat.2016.02.014>
- [21] T. Mukherjee, V. Manvatkar, A. De, T. DebRoy, Dimensionless numbers in additive manufacturing, *J. Appl. Phys.* 121 (2017) 064904. <https://doi.org/10.1063/1.4976006>
- [22] C. Panwisawas, B. Perumal, R.M. Ward, N. Turner, R.P. Turner, J.W. Brooks, H.C. Basoalto, Keyhole formation and thermal fluid flow-induced porosity during laser fusion welding in titanium alloys: Experimental and modelling, *Acta Mater.* 126 (2017) 251-263. <http://dx.doi.org/10.1016/j.actamat.2016.12.062>
- [23] C. Panwisawas, C. Qiu, M.J. Anderson, Y. Sovani, R.P. Turner, M.M. Attallah, J.W. Brooks, H.C. Basoalto, Mesoscale modelling of selective laser melting: Thermal fluid dynamics and microstructural evolution, *Comput. Mater. Sci.* 126 (2017) 479-490. <http://dx.doi.org/10.1016/j.commatsci.2016.10.011>
- [24] C. Panwisawas, Y. Sovani, R.P. Turner, J.W. Brooks, H.C. Basoalto, I. Choquet, Modelling of thermal fluid dynamics for fusion welding, *J. Mater. Process Tech.* 252 (2018) 176-182. <http://dx.doi.org/10.1016/j.jmatprotec.2017.09.019>
- [25] H.C. Basoalto, C. Panwisawas, Y. Sovani, M.J. Anderson, R.P. Turner, B. Saunders, J.W. Brooks, A computational study on the three-dimensional printability of precipitate strengthened nickel-based superalloys, *Proc. R. Soc. A* 474-2220 (2018) 20180295. <http://dx.doi.org/10.1098/rspa.2018.0295>
- [26] H. Chen, W. Yan, Spattering and denudation in laser powder bed fusion process: Multiphase flow modelling, *Acta Mater.* 196 (2020) 154-167. <https://doi.org/10.1016/j.actamat.2020.06.033>
- [27] P.S. Cook, A.B. Murphy, Simulation of melt pool behaviour during additive manufacturing: Underlying physics and progress, *Addit. Manuf.* 31 (2020) 100909. <https://doi.org/10.1016/j.addma.2019.100909>
- [28] Y. Zhao, K. Aoyagi, K. Yamanaka, A. Chiba, A Role of operating and environmental conditions in determining molten pool dynamics during electron beam melting and selective laser melting,

- Addit. Manuf. 36 (2020) 101559. <https://doi.org/10.1016/j.addma.2020.101559>
- [29] P. Stavropoulos, G. Chryssolouris, Molecular dynamics simulations of laser ablation: The Morse potential function approach, *Int. J. Nanomanuf.* 1 (2007) 736-750.
<https://doi.org/10.1504/IJNM.2007.017992>
- [30] P. Stavropoulos, A. Papacharalampopoulos, L. Athanasopoulou, A molecular dynamics based digital twin for ultrafast laser material removal processes, *Int. J. Adv. Manuf. Technol.* 108 (2020) 413-426. <https://doi.org/10.1007/s00170-020-05387-7>
- [31] Y. Lu, K.K. Jones, Z. Gan, W.K. Liu, Adaptive hyper reduction for additive manufacturing thermal fluid analysis, *Comput. Methods Appl. Mech. Engrg.* 372 (2020) 113312.
<https://doi.org/10.1016/j.cma.2020.113312>
- [32] S. Lin, Z. Gan, J. Yan, G.J. Wagner, A conservative level set method on unstructured meshes for modeling multiphase thermo-fluid flow in additive manufacturing processes, *Comput. Methods Appl. Mech. Engrg.* 372 (2020) 113348. <https://doi.org/10.1016/j.cma.2020.113348>
- [33] M.H. Dao, J. Lou, Simulations of laser assisted additive manufacturing by smoothed particle hydrodynamics, *Comput. Methods Appl. Mech. Engrg.* 373 (2021) 113491.
<https://doi.org/10.1016/j.cma.2020.113491>
- [34] G. Zhang, J. Chen, M. Zheng, Z. Yan, X. Lu, X. Lin, W. Huang, Element vaporization of Ti-6Al-4V alloy during selective laser melting, *Metals* 10 (2020) 435.
<https://doi.org/10.3390/met10040435>
- [35] M. Elahinia, N.S. Moghaddam, M.T. Andani, A. Amerinatanzi, B.A. Bimber, R.F. Hamilton, Fabrication of NiTi through additive manufacturing: A review, *Prog. Mater. Sci.* 83 (2016) 630-663. <http://dx.doi.org/10.1016/j.pmatsci.2016.08.001>
- [36] Y.F. Ye, Q. Wang, J. Lu, C.T. Liu, Y. Yang, High-entropy alloy: challenges and prospects, *Mater. Today* 19 (2016) 349-362. <https://doi.org/10.1016/j.mattod.2015.11.026>
- [37] T.F. Flint, L. Scotti, H.C. Basoalto, M.C. Smith, A thermal fluid dynamics framework applied to multi-component substrates experiencing fusion and vaporisation state transitions, *Commun. Phys.* 3 (2020) 196. <https://doi.org/10.1038/s42005-020-00462-7>
- [38] J. Shinjo, A. Umemura, Simulation of liquid jet primary breakup: dynamics of ligament and

- droplet formation, *Int. J. Multiphase Flow* 36 (2010) 513-532.
<https://dx.doi.org/10.1016/j.ijmultiphaseflow.2010.03.008>
- [39] J. Shinjo, J. Xia, L.C. Ganippa, A. Megaritis, Puffing-enhanced fuel/air mixing of an evaporating n-decane/ethanol emulsion droplet and a droplet group under convective heating, *J. Fluid Mech.* 793 (2016) 444-476. <https://dx.doi.org/10.1017/jfm.2016.130>
- [40] J. Shinjo, J. Xia, L.C. Ganippa, A. Megaritis, Physics of puffing and microexplosion of emulsion fuel droplets, *Phys. Fluids* 26 (2014) 103302. <https://dx.doi.org/10.1063/1.4897918>
- [41] J. Shinjo, A. Umemura, Droplet/turbulence interaction and early flame kernel development in an autoigniting realistic dense spray, *Proc. Combust. Inst.* 34 (2013) 1553-1560.
<https://dx.doi.org/10.1016/j.proci.2012.05.074>
- [42] J. Shinjo, J. Xia, A. Megaritis, L.C. Ganippa, R.F. Cracknell, Modeling temperature distribution inside an emulsion fuel droplet under convective heating: A key to predicting microexplosion and puffing, *Atom. Sprays* 26 (2016) 551-583. <https://dx.doi.org/10.1615/AtomizSpr.2015013302>
- [43] G.X. Xu, C.S. Wu, G.L. Qin, X.Y. Wang, S.Y. Lin, Adaptive volumetric heat source models for laser beam and laser + pulsed GMAW hybrid welding processes, *Int. J. Adv. Manuf. Technol.* 57 (2011) 245-255. <https://dx.doi.org/10.1007/s00170-011-3274-x>
- [44] M. Sussman, P. Smereka, S. Osher, A level set approach for computing solutions to incompressible two-phase flow, *J. Comput. Phys.* 114 (1994) 146-159.
<https://doi.org/10.1006/jcph.1994.1155>
- [45] S. Tanguy, T. Menard, A. Berlemont, A level set method for vaporizing two-phase flows, *J. Comput. Phys.* 221 (2007) 837-853. <https://doi.org/10.1016/j.jcp.2006.07.003>
- [46] T. Yabe, F. Xiao, T. Utsumi, The constrained interpolation profile method for multiphase analysis, *J. Comput. Phys.* 169 (2001) 556-593. <https://doi.org/10.1006/jcph.2000.6625>
- [47] J. Shinjo, A. Umemura, Fluid dynamic and autoignition characteristics of early fuel sprays using hybrid atomization LES, *Combust. Flame* 203 (2019) 313-333.
<https://doi.org/10.1016/j.combustflame.2019.02.009>
- [48] P.A. Hooper, Melt pool temperature and cooling rates in laser powder bed fusion, *Addit. Manuf.* 22 (2018) 548-559. <https://doi.org/10.1016/j.addma.2018.05.032>

- [49] C. Panwisawas, Y.T. Tang, J. Ghossoub, R.C. Reed, Additive manufacturability of Nickel-based superalloys: Composition-process induced vapourization, In: S. Tin *et al.* (eds.) Superalloys 2020. The Minerals, Metals & Materials Series. Springer, Cham. (2020)
https://doi.org/10.1007/978-3-030-51834-9_100
- [50] Y.T. Tang, C. Panwisawas, J. Ghossoub, Y. Gong, J. Clark, A. Németh, D.G. McCartney, R.C. Reed, Alloys-by-design: Application to new superalloys for additive manufacturing, *Acta Mater.* 203 (2020) 116468. <https://doi.org/10.1016/j.actamat.2020.09.023>
- [51] J. Trapp, A.M. Rubenchik, G. Guss, M.J. Matthews, In situ absorptivity measurements of metallic powders during laser powder-bed fusion additive manufacturing, *Appl. Mater. Today* 9 (2017) 341-349. <https://doi.org/10.1016/j.apmt.2017.08.006>
- [52] A.H. Persad, C.A. Ward, Expressions for the evaporation and condensation coefficients in the Hertz-Knudsen relation, *Chem. Rev.* 116 (2016) 7727-7767.
<https://doi.org/10.1021/acs.chemrev.5b00511>
- [53] NIST Chemistry WebBook, National Institute of Standards and Technology, USA
(<https://webbook.nist.gov/chemistry/>) Accessed Feb. 2020
- [54] AIST Thermophysical Properties Database System, National Institute of Advanced Industrial Science and Technology, Japan (<https://tpds.db.aist.go.jp/tpds-web/index.aspx>) Accessed Feb. 2020
- [55] T. Iida, Physical properties of liquid metals IV, *J. Japan Welding Soc.*, 63 (1994) 140-145.
- [56] Y. Waseda, M. Ohtani, The estimation of viscosity coefficient, self-diffusion coefficient, and surface tension of molten metals by the principle of corresponding state, *Tetsu-to-Hagane* 61 (1975) 46-53.
- [57] P.-F. Paradis, T. Ishikawa, S. Yoda, Non-contact measurements of surface tension and viscosity of niobium, zirconium, and titanium using an electrostatic levitation furnace, *Int. J. Thermophys.* 23 (2002) 825-842. <https://doi.org/10.1023/A:1015459222027>
- [58] T. Iida, R. Guthrie, M. Isac, N. Tripathi, Accurate predictions for the viscosities of several liquid transition metals, plus barium and strontium, *Metall. Mater. Trans. B* 37B (2006) 403-412.
<https://doi.org/10.1007/s11663-006-0025-8>

- [59] P.-F. Paradis, T. Ishikawa, R. Fujii, S. Yoda, Thermophysical properties of molten tungsten measured with an electrostatic levitator, *Heat Trans.-Asian Res.* 35 (2006) 152-164.
- [60] P.-F. Paradis, T. Ishikawa, N. Koike, Non-contact measurements of the surface tension and viscosity of molybdenum using an electrostatic levitation furnace, *Int. J. Refract. Met. H.* 25 (2007) 95-100. <https://doi.org/10.1016/j.ijrmhm.2006.02.001>
- [61] P.-F. Paradis, W.-K. Rhim, Thermophysical properties of zirconium measured using electrostatic levitation, *Proc. SPIE 3792, Mater. Res. Low Gravity II*, (1999).
- [62] J.T. Okada, T. Ishikawa, Y. Watanabe, P.-F. Paradis, Surface tension and viscosity of molten vanadium measured with an electrostatic levitation furnace, *J. Chem. Thermodyn.* 42 (2010) 856-859. <https://doi.org/10.1016/j.jct.2010.02.008>
- [63] P.-F. Paradis, T. Ishikawa, S. Yoda, Surface tension and viscosity of liquid and undercooled tantalum measured by a containerless method, *J. Appl. Phys.* 97 (2005) 053506. <https://doi.org/10.1063/1.1854211>
- [64] P.-F. Paradis, S. Yoda, T. Ishikawa, Y. Saita, Thermophysical properties of liquid and supercooled ruthenium measured by noncontact methods, *J. Mater. Res.* 19 (2004) 590-594. <https://doi.org/10.1557/jmr.2004.19.2.590>
- [65] B.J. Keene, Review of data for the surface tension of pure metals, *J. Int. Mater. Rev.* 38 (1993) 157-192. <https://doi.org/10.1179/imr.1993.38.4.157>
- [66] Y. Waseda, M. Ohtani, Structure and effective interionic potential of liquid palladium, platinum and zirconium, *Z. Physik B* 21 (1975) 229-234.
- [67] T. Ishikawa, P.-F. Paradis, S. Yoda, Noncontact surface tension and viscosity measurements of rhenium in the liquid and undercooled states, *Appl. Phys. Lett.* 85 (2004) 5866. <https://doi.org/10.1063/1.1836002>
- [68] A.K. Roy, R.P. Chhabra, Prediction of solute diffusion coefficients in liquid metals, *Metall. Trans. A* 19A (1988) 273-279.
- [69] M. Courtois, M. Carin, P. Le Masson, S. Gaied, M. Balabane, A new approach to compute multi-reflections of laser beam in a keyhole for heat transfer and fluid flow modelling in laser welding, *J. Phys. D: Appl. Phys.* 46 (2013) 505305. <https://doi.org/10.1088/0022-3727/46/50/505305>

- [70] S.-W. Han, J. Ahn, S.-J. Na, A study on ray tracing method for CFD simulations of laser keyhole welding: progressive search method, *Weld World* 60 (2016) 247-258.
<https://doi.org/10.1007/s40194-015-0289-1>